Effect of δ-ferrite on impact properties of supermartensitic stainless steel heat affected zones

D. Carrouge, H. K. D. H. Bhadeshia and P. Woollin

The work presented in this paper focuses on the effect of the presence of non-equilibrium δ-ferrite on the impact properties of a supermartensitic stainless steel. To generate homogeneous δ-ferrite containing microstructures the material was, in the first part of the present study, subjected to a series of high temperature furnace heat treatments. Three microstructures possessing variable ferrite content and different grain sizes were generated. Charpy impact results indicate that the presence of 14% δ-ferrite in a martensitic matrix of 60 μm prior austenite grain size, raises the ductile to brittle transition temperature (DBTT) by about 50°C compared with a fully martensitic microstructure of 80 μm. For a similar grain size, reducing the amount of δ-ferrite from 14 to 2% restored the DBTT to a level comparable to that of the tempered parent material. A Gleeble simulator was used to create the range of microstructures found in a weld heat affected zone (HAZ). Testing of the simulated HAZ indicated that toughness was not significantly affected by the presence of δ-ferrite. The DBTT was comparable to that of the parent material and lower than that of the heat treated specimens containing 14% δ-ferrite. STWJ/410

Keywords: supermartensitic stainless steels, weld heat affected zone, delta-ferrite toughness

At the time this work was carried out Dr Carrouge and Professor Bhadeshia were in the Department of Materials Science and Metallurgy, University of Cambridge, Pembroke Street, Cambridge CB2 3QZ, UK. Dr Carrouge is now with Corus plc. Dr Woollin is with TWI Ltd, Granta Park, Great Abington, Cambridge, UK. *Manuscript received 3 December 2002; accepted 27 May 2003.*

INTRODUCTION

Supermartensitic stainless steels have recently been introduced in the oil and gas industry to substitute more expensive duplex (ferritic-austenitic) stainless steels for onshore and offshore tubing applications. The optimised microstructure of the material is free from δ-ferrite and offers good corrosion resistance in environments containing CO_2 and some H_2S. In addition to reducing carbide precipitation, the low carbon content (i.e. about 0·01 wt-%) of supermartensitic steels provides good weldability with conventional arc welding techniques.

Recent studies of the phase transformation occurring in the HAZ of the welded material revealed the presence of small amounts of δ-ferrite in the high temperature regions of the HAZ.[1,2] While it is well established that coarse δ-ferrite grains strongly reduce the Charpy notch toughness of low carbon semi-ferritic and martensitic stainless steels,[3–5] there is as yet no evidence to support the contention that the δ-ferrite found in supermartensitic stainless steel heat affected zones has such a pronounced effect. Consequently, the aim of the present study was to assess whether the presence of δ-ferrite in supermartensitic steels significantly affects the impact properties of the HAZ.

Charpy impact testing has been chosen to evaluate the impact properties of a series of microstructures. The first part of this work concentrates on microstructures generated using furnace heat treatments. The other part focuses on HAZ that have been simulated using a Gleeble weld-simulator.

Material studied

Steel A whose chemical composition is reported in Table 1, is a highly alloyed supermartensitic stainless steel stabilised by the addition of titanium. The stabilisation works by forming stable carbonitrides Ti(C, N), thereby decreasing the carbon or nitrogen in solid solution and preventing the precipitation of chromium or molybdenum carbonitrides which may lead to a reduction in the corrosion resistance.[6] The minimum titanium content required to prevent these effects is four times the carbon plus nitrogen concentration (wt-%) owing to the stoichiometry of Ti(C, N). Steels of composition similar to that of steel A have been reported to have a martensite start temperature M_s of about 200°C; the alloy transforms entirely to martensite during cooling from the solution temperature.[7]

The material was supplied as a seamless pipe of 273·1 mm outer dia. and 12·0 mm wall thickness. A study revealed this steel to be prone to HAZ δ-ferrite retention.[1,8,9]

Phase balance and transformation temperatures

Equilibrium calculations using MT-DATA software have been conducted on steel A to determine the phase balance and phase transformation temperatures. MT-DATA uses experimentally determined parameters to model thermodynamic variables. For this reason, the reliability of the calculations it performs depends on the parameters present in the databases. Simpler systems are more accurately predicted by MT-DATA; hence, only the elements in major

Table 1 Chemical composition of steel A, wt-%

C	0·01
Si	0·26
Mn	0·46
Ni	6·46
Cr	12·20
Mo	2·48
Cu	0·03
Ti	0·09
N	0·0070

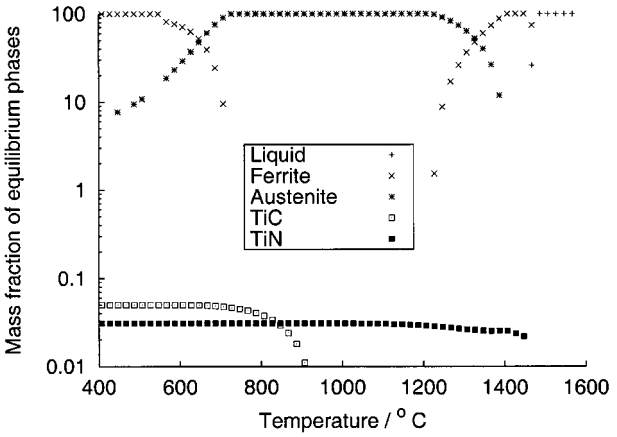

1 Result of MT-DATA equilibrium calculation performed on steel A

quantities are taken into account in calculations. The latter were made without silicon since MT-DATA has been found to give silicon an excessively strong ferrite-forming tendency in the systems of concern. The most important elements, phases, common carbides and nitrides have been allowed and are listed in Table 2.

Calculations have been performed over the temperature range 400–1600°C at intervals of 25°C using the *plus* and *sub-sgte* databases. Figure 1 shows the evolution of the mass fractions of the equilibrium phases as a function of temperature. Steel A is predicted to have the capacity to become fully austenitic and then undergo complete ferritisation before melting. As a result of the presence of titanium, the precipitation of carbides and nitrides is restricted to TiC and TiN particles. Titanium carbides are predicted to dissolve at temperatures close to 900°C.

Table 3 reports the predicted equilibrium phase transformation temperatures. Under equilibrium conditions, the Ae_1 temperature is lower than 400°C owing to the relatively high nickel content of the steel. Ferrite starts forming at 1237°C and the ferritisation interval is 159°C. The latter interval is relatively large mainly as a result of the strong ferrite stabilising effect of molybdenum.

IMPACT PROPERTIES OF HEAT TREATED SPECIMENS

The impact properties of the parent material in its as-received condition were first studied. Then, to investigate the effect of δ-ferrite on the ductile to brittle temperature (DBTT), fully martensitic and ferritic-martensitic microstructures were required. The results of a preliminary study revealed that furnace heat treatments at 1100°C and 1350°C for 15 min were satisfactory to produce the desired

Table 2 List of elements and phases used for equilibrium calculation performed on steel A

Alloy	Allowed elements	Allowed phases
A	Fe, C, Mn, Ni, Cr, Mo, Ti, N	$M_{23}C_6$, γ, δ, Fe_3C, M_7C_3, TiC, TiN, Liq

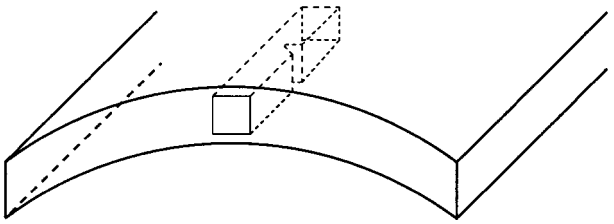

2 Orientation of Charpy specimen within pipe

microstructures.[9] However, to facilitate the interpretation of Charpy transition curves, a difference in prior austenite grain size between specimens heat treated at different temperatures is not advisable. To study the impact properties at a given grain size, the ferritic-martensitic microstructure was re-austenitised to dissolve ferrite.

Procedure and experimental techniques

Forty specimens of 12 mm square section and 60 mm long were machined from steel A in the longitudinal direction as shown in Fig. 2. Ten specimens were kept in the as-received state (quenched from 950°C and tempered at 640°C). Thirty other samples were individually placed in a preheated furnace at the centre of the bottom surface and were left in for 15 min followed by water quenching. Using this procedure, 10 specimens were heat treated at 1100°C and 20 others at 1350°C. After cooling, 10 of the latter specimens were re-austenitised at 1100°C for an hour and then water quenched. Four different microstructures were therefore produced.

To reveal the microstructures, specimens were ground on SiC paper to grit 1200 and polished with a 1 μm cloth coated with diamond paste. The samples were etched using one of the two etchants listed in Table 4. Digital photographs were taken using a Leica DMR digital camera.

The volume fractions of δ-ferrite in the specimens have been determined using SigmaScan Pro 5·0 software using the following procedure. A series of digital micrographs were taken from representative areas of the specimens. The images were first enhanced to use the full intensity spectrum and the total number of pixels in the image was determined. To highlight δ-ferrite, the intensity threshold method was employed and the sum of pixels constituting the selected features was performed. The ratio of the latter sum with the original number of pixels led to the determination of the volume fraction.

To investigate the presence of any retained austenite (γ_r) in the different specimens, X-ray diffraction tests were

Table 3 Equilibrium phase transformation temperatures (°C) obtained after calculations performed on steel A

Alloy	Ae_1 (5%)	Ae_3 (95%)	Ae_4 (5%)	Ae_5 (95%)	Solidus (5%)
A	<400	705	1237	1396	1461

Ae_1, Ae_4 and solidus temperatures have been obtained by taking temperature at which 5% of growing phase has formed. Similarly, Ae_3 and Ae_5 temperatures have been obtained by taking temperature at which 95% of growing phase has formed.

Table 4 Compositions and conditions of use of etchants

Name	Composition	Etching procedure	Specificity
Sulphuric[10]	20 mL H_2SO_4 0·01 g NH_4CNS 80 mL H_2O	Immersion of sample and electrolytic etching at 4 V for 20 s	Reveals δ-ferrite but not martensite
Stock[11]	1 g $K_2S_2O_5$ 20 mL HCl 80 mL H_2O	Immersion of sample until specimens becomes red	Reveals δ-ferrite in blue and martensite yellow/brown

carried out. The latter were performed on a Phillips diffractometer using Cu K_α radiation operating at 40 kV and 40 mA. Step scan mode was employed to cover the angular 2θ range from 47·1 to 103°. The 2θ step size was 0·05° with a dwell time of 30 s. Samples were ground and polished using the normal metallographic preparation procedure with two cycles of polishing and etching before the X-ray diffraction test to remove any deformed layer caused by polishing. The diffraction peaks were indexed by comparing theoretical to experimental interplanar spacing values for ferrite and austenite planes.

The volume fraction of austenite was estimated from measurements of the integrated intensities of martensite and austenite peaks assuming they are the only phases present.

As the volume fractions are measured from the intensities, which are corrected for the structure and other systematic factors, the patterns obtained did not require calibration.[12] The ratio of the intensities of diffraction peaks from two phases of a polycrystalline sample is given by equation (1)[12]

$$\frac{I_{\gamma(\mathrm{hkl})}}{I_{\alpha'(\mathrm{hkl})}} = \frac{R_{\gamma(\mathrm{hkl})}}{R_{\alpha'(\mathrm{hkl})}} \times \frac{V_\gamma}{V_{\alpha'}} \quad \ldots\ldots\ldots\ldots (1)$$

where $I_{\gamma(\mathrm{hkl})}$ and $I_{\alpha'(\mathrm{hkl})}$ are the integrated intensity from a given plane (hkl) from the austenite and martensite (or ferrite) phase, respectively. V_γ and $V_{\alpha'}$ are the volume fractions of austenite and martensite, respectively, and $R_{\gamma\ (\mathrm{hkl})}$ and $R_{\alpha'(\mathrm{hkl})}$ are given for a specific peak by

$$R = \frac{1}{v^2}\ [|F|^2(p)(L_\mathrm{p})]e^{-2\mathrm{m}} \quad \ldots\ldots\ldots\ldots (2)$$

where v=volume of unit cell, F=structure factor, p=multiplicity factor, L_p=Lorentz-polarisation factor, and $e^{-2\mathrm{m}}$=temperature factor.

Considering that all materials in reality exhibit crystallographic texture, the average integrated intensity for at least three specific reflections for austenite and martensite (Table 5) were taken into account (equations (3) and (4)).

$$\frac{I_\gamma}{R_\gamma} = \frac{1}{3}\sum_{\mathrm{i}=1}^{3}\frac{I_\mathrm{i}^\gamma}{R_\mathrm{i}^\gamma} \quad \ldots\ldots\ldots\ldots (3)$$

$$\frac{I_{\alpha'}}{R_{\alpha'}} = \frac{1}{3}\sum_{\mathrm{i}=1}^{3}\frac{I_\mathrm{i}^{\alpha'}}{R_\mathrm{i}^{\alpha'}} \quad \ldots\ldots\ldots\ldots (4)$$

The value of $V_\gamma/V_{\alpha'}$ in equation (1) can be obtained from the measurement of $I_\gamma/I_{\alpha'}$ and the calculation of $R_\gamma/R_{\alpha'}$. Once $V_\gamma/V_{\alpha'}$ is found, the value of V_γ can be obtained from the additional relationship

$$V_\gamma + V_{\alpha'} = 1 \quad \ldots\ldots\ldots\ldots (5)$$

The 2θ values for three austenite peaks were used to calculate the d spacings with Bragg's law and then the lattice parameter a. These values were plotted against $\sin^2\theta$. An accurate value of a_γ was found by extrapolation to $\sin^2\theta = 1$.[12]

To study the location of any retained austenite, a JEOL 200 CX transmission electron microscope (TEM) operating at 200 kV has been used. Thin foils of 3 mm dia. and approximately 50 μm thick were obtained from the specimens employed for X-ray analysis. The discs were electropolished in a solution of 5% perchloric acid, 15% glycerol and 80% ethanol at an applied voltage of 50 V at room temperature. Conventional selected-area diffraction was used to distinguish austenite (fcc structure) from low carbon martensite (bcc).

Table 5 Diffracting *hkl* planes used for martensite and austenite

Phase *i*	Diffracting plane (*hkl*)
Martensite 1	200
Martensite 2	211
Martensite 3	220
Austenite 1	200
Austenite 2	220
Austenite 3	311

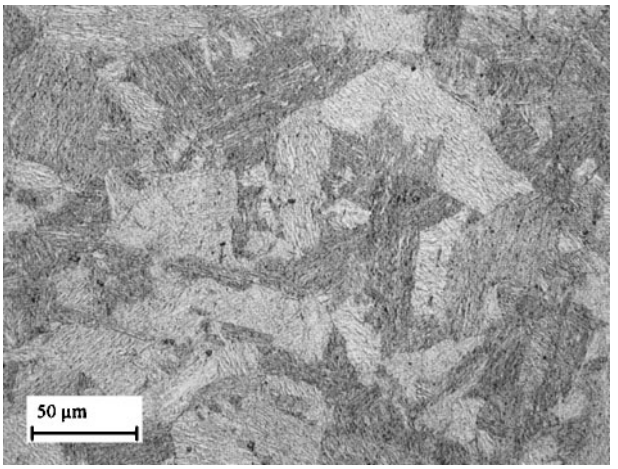

3 Optical micrograph of initial microstructure of steel A, electrolytically etched

After optical verification of the desired microstructures, the heat treated specimens were machined to the standard dimension of 10 mm square section × 55 mm with a 2 mm deep V-notch positioned through-thickness at the middle of the specimens. Charpy impact tests were finally carried out in accordance with British Standard 10045-1[13] between 20 and −200°C to reveal any ductile–brittle transition.

The fracture surfaces of Charpy specimens were observed using a JEOL 5800 scanning electron microscope (SEM). Secondary electron mode was employed at an accelerating voltage of 15 kV. To identify the nature of particles, micro-analytical experiments were carried out using an energy dispersive X-ray (EDX) analysis system. ZAF (atomic number, absorption, fluorescence) corrections were employed, the acquisition time was set to 100 s and the dead time was kept below 20%.

As-received microstructure

The initial microstructure of the material electrolytically etched, is shown in Fig. 3. It consisted of tempered martensite with no evidence of δ-ferrite and some apparent titanium carbonitride particles.

X-ray diffraction tests revealed that steel A contained a significant amount of retained austenite (Fig. 4). The volume percentage of the latter was 13% within an experimental error of ±0·5%. The error calculation was based on the integrated intensity since this error is characteristic of the specimen studied.

This austenite remained stable after immersion in liquid nitrogen for 30 min, but after re-austenitisation at 1000°C for 30 min and water quenching, no austenite could be detected (Fig. 5). Those results indicated that the presence of retained austenite in the as-received condition was the consequence of the manufacturer's tempering treatment. In fact, tempering must have been carried out a few degrees above the steel Ac_1 temperature. In this case, the new austenite is significantly enriched in carbon and nickel and remains stable after cooling.[7]

A TEM examination of a thin foil prepared on steel A showed this retained austenite to be present as small elongated grains located at martensite lath boundaries as illustrated in Fig. 6.

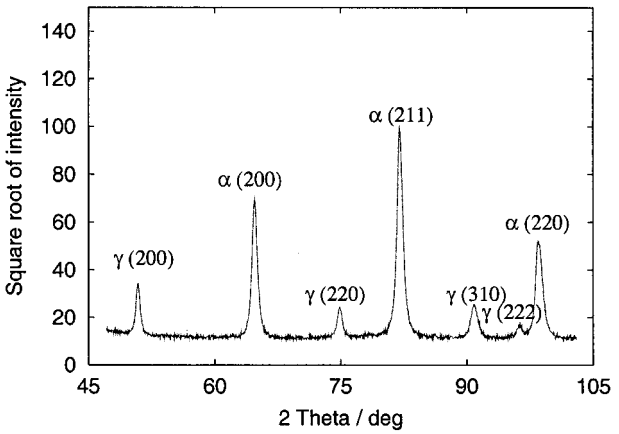

4 X-ray diffraction pattern of steel A in as-received condition

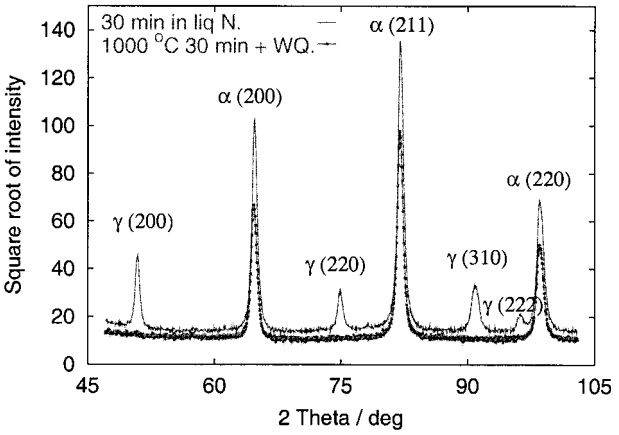

5 X-ray diffraction pattern of steel A after indicated thermal treatment (WQ: water quench)

Characterisation of heat treated specimens

To facilitate the interpretation of the results, heat treated specimens were characterised before impact testing in terms of phase presence, volume fraction, hardness and grain size.

Figure 7 shows the microstructures of the fully martensitic, martensitic/ferritic and annealed martensitic/ferritic specimens observed on the actual-size Charpy specimens. Typical cuboid Ti(C,N) precipitates were the only observed non-metallic particles. These particles were up to 10 μm long and occurred in random dispersion or as small distinct clusters.

In the first martensitic/ferritic microstructure, δ-ferrite was located both at grain boundaries and within the grains. Its volume percentage measured by image analysis at a magnification of 200 was $14 \pm 2\%$. Complete re-austenitisation of the latter microstructure gave a reduction of the δ-ferrite content to $2 \pm 0{\cdot}5\%$ and spheroidisation of the remaining ferrite. The dissolution of δ-ferrite appeared to be a slow process since 2% ferrite were still present after an hour at 1100°C. This is because significant partitioning of substitutional solutes occurred at 1350°C as indicated by the EDX measurements reported in Table 6.

Table 6 Summary of 15 EDX microanalyses (wt-%) performed on ferrite and martensite

	Composition		
Phase	Cr	Ni	Mo
δ-ferrite	$13{\cdot}5 \pm 0{\cdot}9$	$4{\cdot}8 \pm 1{\cdot}0$	$2{\cdot}6 \pm 0{\cdot}4$
Matrix	$11{\cdot}7 \pm 0{\cdot}3$	$7{\cdot}0 \pm 0{\cdot}4$	$1{\cdot}7 \pm 0{\cdot}2$

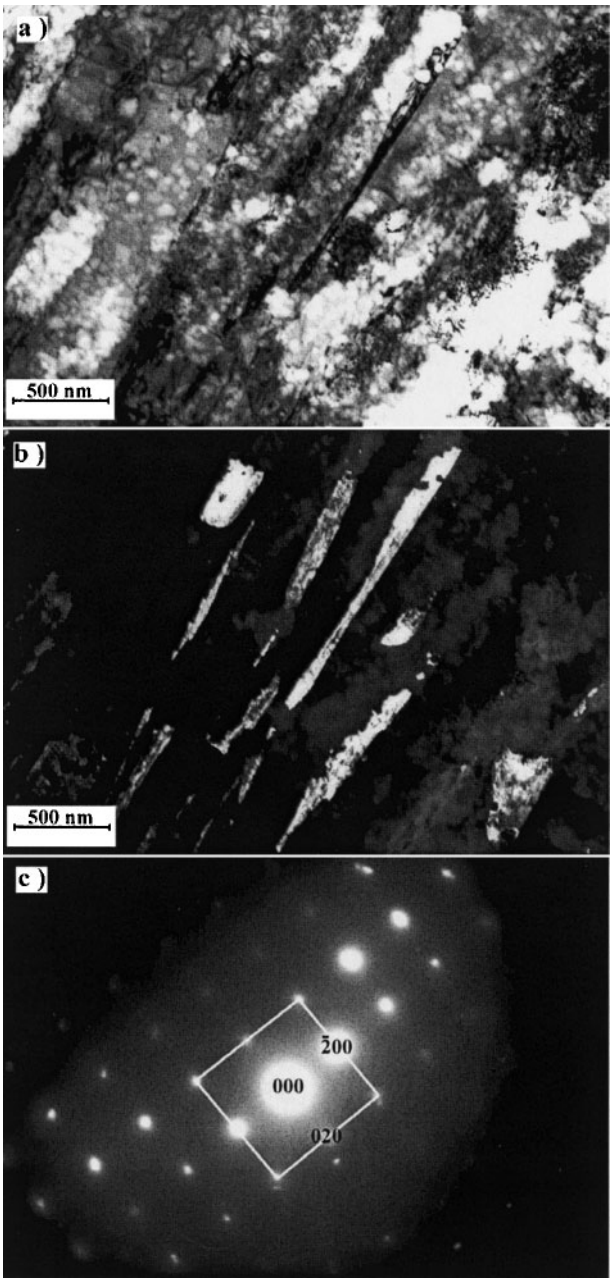

6 *a* Bright field image of martensite plus retained austenite region; *b* dark field image of same region as *a*; *c* selected area diffraction pattern of austenite corresponding to dark field image

There were no apparent differences in the microstructure in terms of Ti(C,N) particles. This was expected since the ferritising and the re-austenitising operations were performed above the predicted temperature of TiC dissolution (about 900°C) and water quenching prevents precipitation during cooling.

The hardness and grain sizes measured on all materials are reported in Table 7. Despite the presence of 14%

Table 7 Macrohardness (HV10) and grain size of different microstructures

Microstructure	Hardness	Grain size, μm
Tempered martensite + γ_r	296 ± 3	25 ± 4
Fresh martensite	317 ± 8	60 ± 9
Fresh martensite + 14% δ-ferrite	311 ± 8	80 ± 12
Fresh martensite + 2% δ-ferrite	304 ± 7	80 ± 12

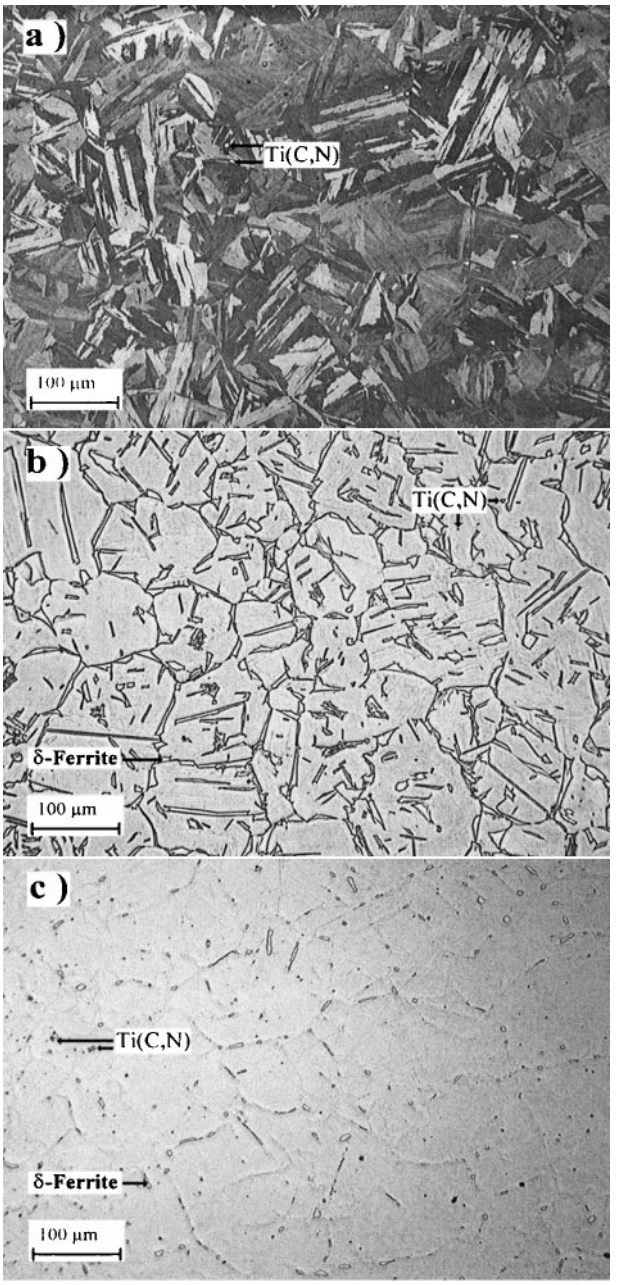

7 Microstructures obtained after isothermal treatment at *a* 1100°C and *b* 1350°C for 15 min and water quenched. *c* Microstructure obtained after treatment at 1350°C for 15 min and water quenched followed by re-austenitisation at 1100°C for 60 min and water quenched

δ-ferrite, there was little hardness change between the different microstructures. The latter was attributed to the virtually carbon free martensite as a result of the presence of titanium in concentrations greater than the stoichiometric amount. As tensile strength is proportional to hardness, all specimens could be assumed to have a similar strength.[14] There was a small difference in grain size between the various microstructures. In fact, the prior austenite grain size of the specimens heat treated at 1350°C was about 20 μm larger than the one heat treated at 1100°C. As a result of the grain boundary pinning effect of δ-ferrite, there was no grain size difference between the microstructures consisting of fresh martensite and various amounts of ferrite.

The presence of retained austenite in the furnace heat treated specimens has been checked using X-ray diffraction. No austenite could be detected in any of the specimens (Fig. 8).

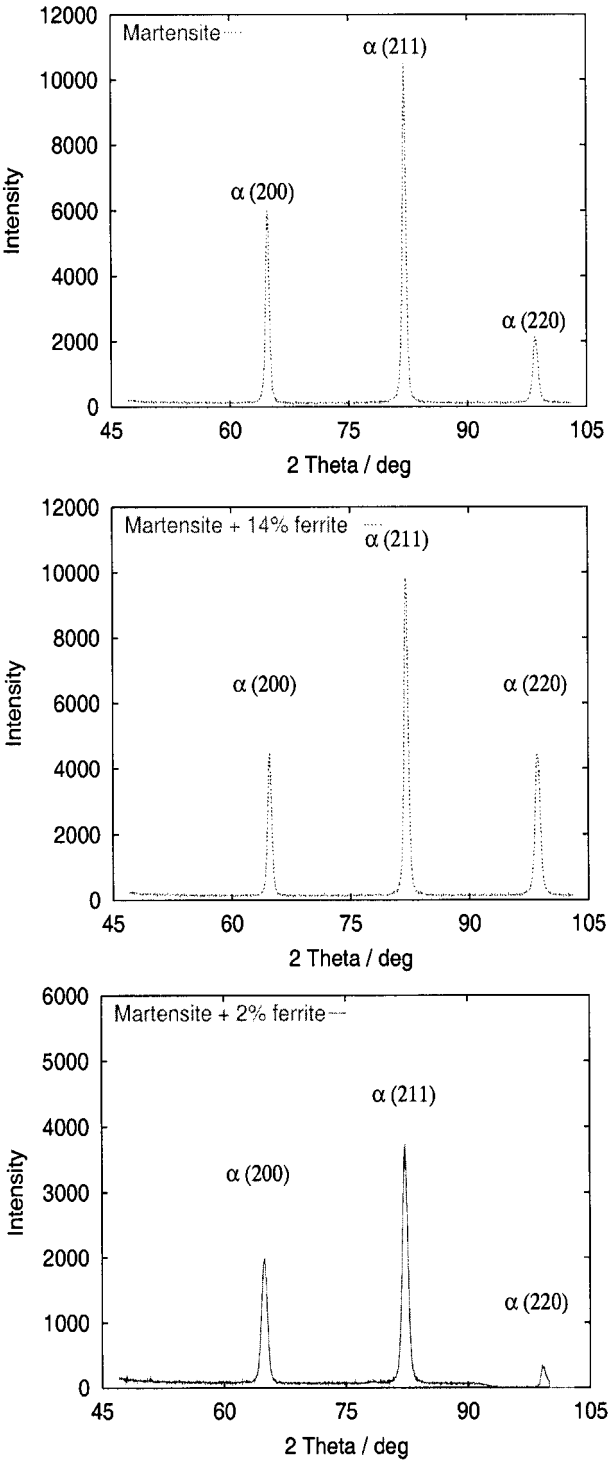

8 X-ray diffraction patterns of fresh martensite, fresh martensite + 14% δ-ferrite and fresh martensite + 2% δ-ferrite microstructures

Results of Charpy impact tests

To facilitate the comparison and the determination of the ductile to brittle transition temperature (DBTT), the toughness results have been fitted by a non-linear regression technique to the equation[15]

$$\text{Impact energy (J)} = A_0 + B_0 \tanh\left(\frac{T - T_0}{C_0}\right) \quad (6)$$

where A_0, B_0, C_0 and T_0 are fitting constants and T is the temperature in °C. The DBTT was taken as the temperature corresponding to half the height of the transition curve. Table 8 summarises the measured ductile

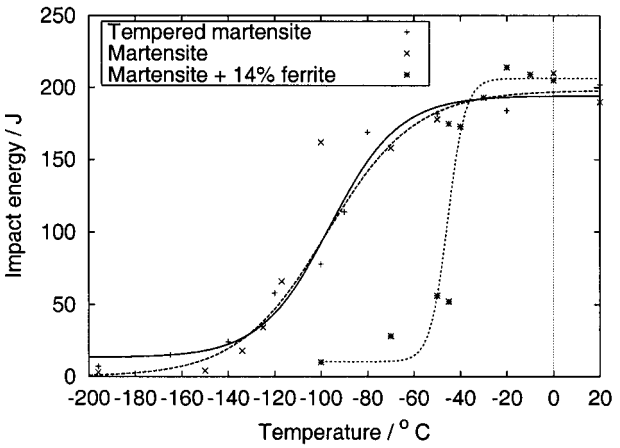

9 Charpy impact energy curves obtained on tempered martensite + retained austenite (as-received condition), fresh martensite and fresh martensite + 14% δ-ferrite microstructures

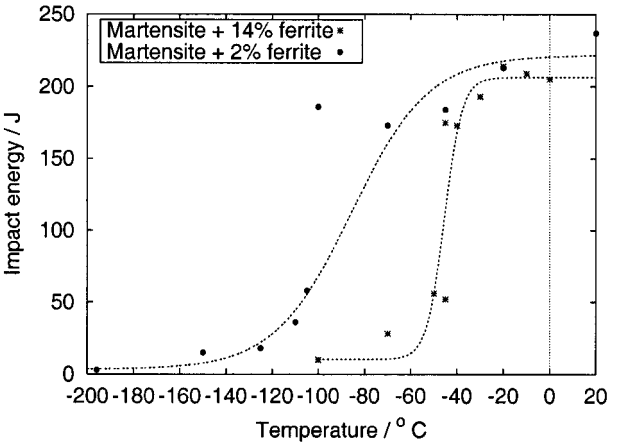

10 Charpy impact energy curves obtained on fresh martensite + 14% δ-ferrite and fresh martensite + 2% δ-ferrite microstructures. Note that both microstructures have identical prior austenite grain size of 80 μm

to brittle transition temperatures for each tested microstructure.

Figure 9 shows the impact transition curves obtained from the tempered martensite + γ_r (as-received condition), fresh martensite and fresh martensite + 14% δ-ferrite microstructures. The transition curves of the as-received and fresh martensite microstructures were similar and their DBTT were identical and far below 0°C. However, the as-received microstructure showed slightly higher failure energies at low temperatures. This is because the retained austenite tends to transform to martensite during impact and thus absorbs some energy and raises the toughness, as proposed by Bilmes *et al.*[16] At room temperature, there was more scatter in the energy required to break the specimens but there was apparently no significant difference between the two microstructures.

Similarly, there were no apparent differences between the upper shelf failure energies of the fresh martensite and fresh martensite + 14% δ-ferrite microstructures (Fig. 9). However, the transition occurred over a shorter temperature range in the biphased microstructure and a significant shift in ductile to brittle transition temperature was observed. In fact, the DBTT of the duplex microstructure was raised by 52°C to about −46°C. The origin of this increase could not be attributed directly to the presence of δ-ferrite since there was a 20 μm difference in prior austenite grain size between the two microstructures.

The observation of the transition curves of the fresh martensite + 14% δ-ferrite and fresh martensite + 2% δ-ferrite microstructures of identical grain size removed this uncertainty (Fig. 10). In fact, specimens containing a reduced amount of δ-ferrite had significantly better DBTT (−86°C compared to −46°C). As mentioned in the previous section, after re-austenitisation and quenching, the only difference between the two ferrite containing microstructures was the actual level of ferrite. Consequently, it was clear that for a prior austenite grain size of 80 μm, the presence of δ-ferrite significantly affected the transition temperature.

Table 8 Ductile to brittle transition temperatures obtained for each microstructure studied

Microstructure	DBTT (°C)
Tempered martensite + γ_r	−98
Fresh martensite	−98
Fresh martensite + 14% δ-ferrite	−46
Fresh martensite + 2% δ-ferrite	−86

Figure 11 compares the transition curves of the fresh martensite + 2% δ-ferrite (grain size 80 μm) with the tempered martensite + γ_r microstructure (grain size 25 μm). The reduction of the ferrite content clearly improves the notch toughness to a level comparable to that of the as-received condition.

Fractography

Observation of the fracture surfaces in the SEM revealed a variety of fracture modes. In particular, ductile rupture, cleavage and quasi-cleavage could be identified. McDonald *et al.* summarise these fracture modes as follows:[17,18]

(i) Ductile rupture. Dimples resulting from microvoid formation and coalescence, are characteristic of ductile rupture. Microvoids are generally initiated at inclusions, which can sometimes be observed within the dimples

(ii) Cleavage. Stepped facets are caused by fracture through regions of different crystallographic orientation. Cleavage occurs by the rapid propagation of a crack along crystallographic planes, and may be initiated by inclusion/matrix decohesion. This is a very low energy-absorbing mode of fracture

(iii) Quasi-cleavage. A less well-defined fracture mode, known as quasi-cleavage, is associated with tear ridges which represent limited plastic deformation separating cleavage facets. Unlike pure cleavage, energy is absorbed as a result of the limited plastic deformation.

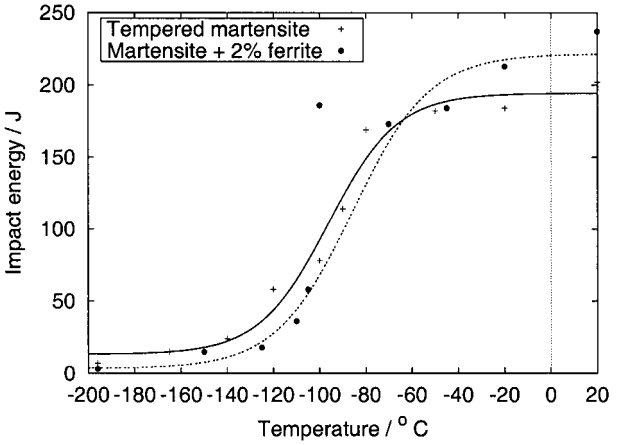

11 Comparison of Charpy impact energy curves between as-received and fresh martensite + 2% δ-ferrite microstructures

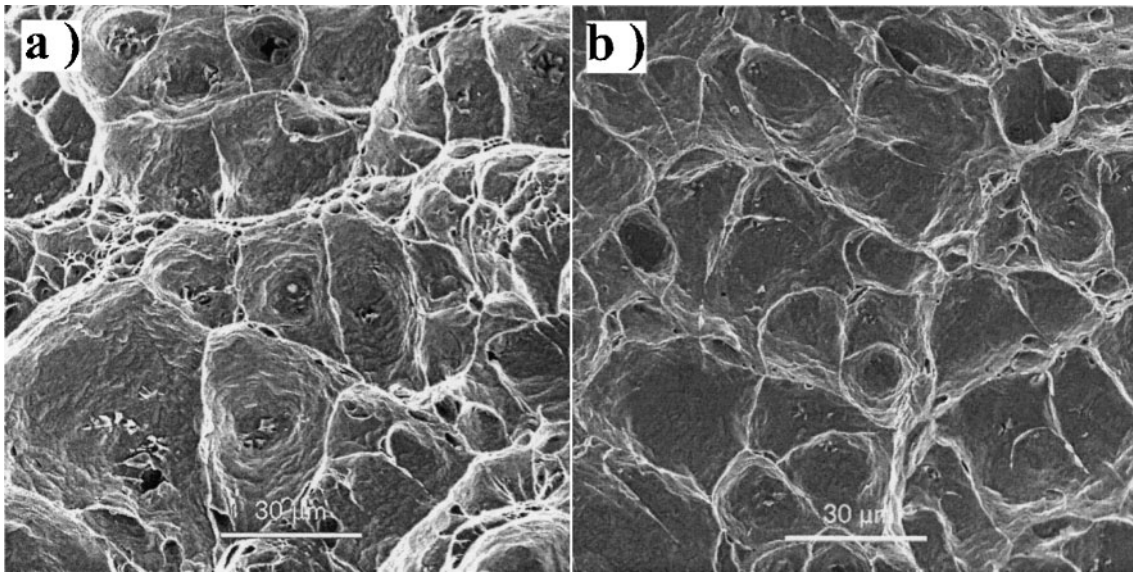

12 Dimpled fracture surfaces of *a* fresh martensite, and *b* fresh martensite + 14% δ-ferrite microstructures tested at 0°C

Examples of ductile rupture obtained from the fully martensitic and martensitic/ferritic microstructures tested at 0°C are shown in Fig. 12. Most cuboidal shaped titanium carbonitride particles were cracked.

Specimens tested at low temperatures fractured in a transgranular manner (Fig. 13). This indicated that the presence of grain boundary δ-ferrite did not embrittle the latter. In general, the cleavage facet sizes appeared similar but the fresh martensite + 14% δ-ferrite microstructure showed more secondary cracks.

River markings on the cleavage facets of the specimens showed evidence of both cleavage (Fig. 14) and quasi-cleavage fracture (Fig. 15) initiated by Ti(C,N) inclusions. The capacity of these particles to reduce toughness is well known. Brittle fracture induced by the cleavage of TiN inclusions has recently been investigated by Fairchild *et al.*[19,20] Those particles are well bonded to the matrix and thus allow high stresses in a notch tip plastic zone to act on inclusions without debonding the interface. Once an inclusion cleaves, the strong bond allows for transfer of the crack into the martensitic matrix.

In addition to the SEM observation, cross-sections perpendicular to the fracture surfaces, as shown in Fig. 16, have been observed to reveal the fracture path. Figures 17 and 18 show example of such cross-sections for specimens of the fresh martensite + 14% δ-ferrite and fresh martensite + 2% δ-ferrite microstructures which failed by cleavage.

In the fresh martensite + 14% δ-ferrite specimens, secondary intragranular cracks propagated through martensite and δ-ferrite stringers, whereas shorter cracks were seen to initiate both in martensite and at the δ-ferrite/martensite interface in the fresh martensite + 2% δ-ferrite. In the latter case, cracks could not easily link up when δ-ferrite was more dispersed and possessed a spheroidised morphology thus explaining the better impact properties.

IMPACT PROPERTIES OF GLEEBLE SIMULATED SPECIMENS

The first part of this work established the effect of δ-ferrite on the ductile to brittle transition temperature of homogenous and biphased microstructures. The microstructure

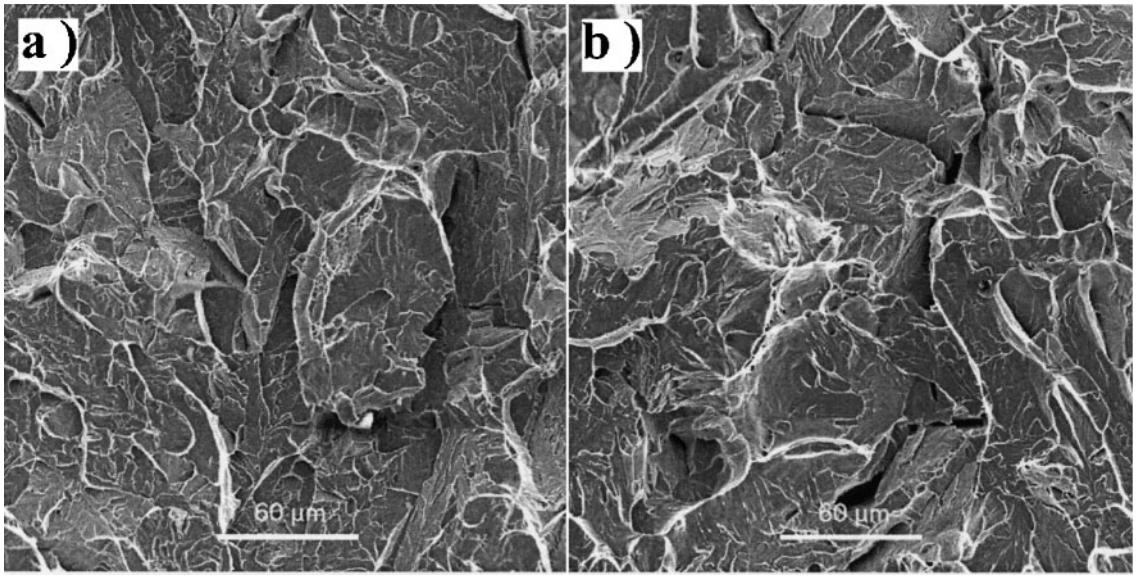

13 Fracture surfaces of *a* fresh martensite and *b* fresh martensite + 14% δ-ferrite microstructures tested at −150 and −100°C, respectively

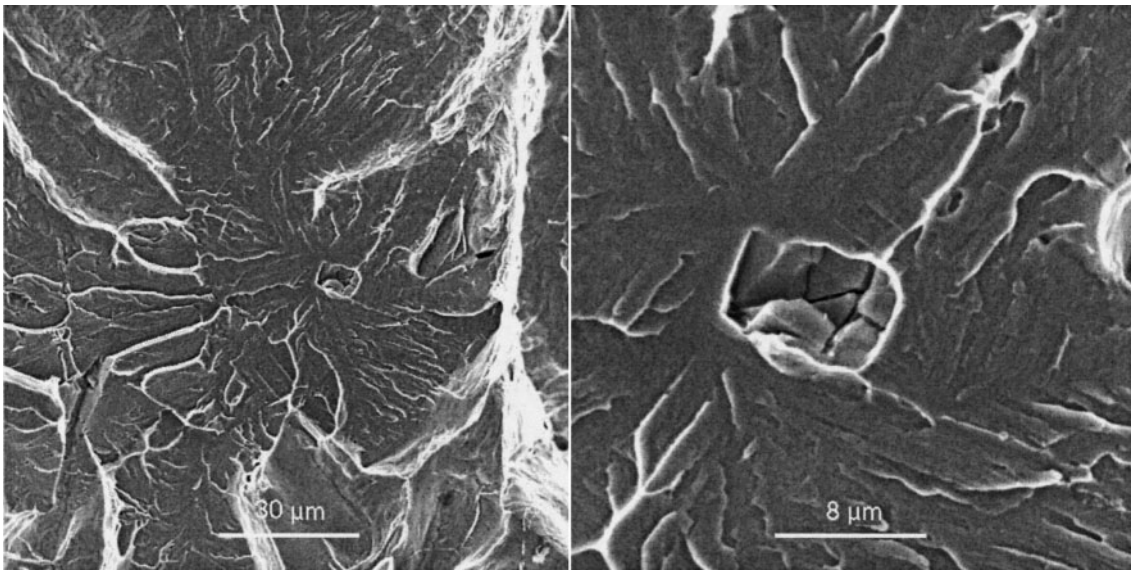

14 Fracture surfaces of fresh martensite + 14% δ-ferrite microstructure tested at −100°C showing Ti(C,N) initiated cleavage

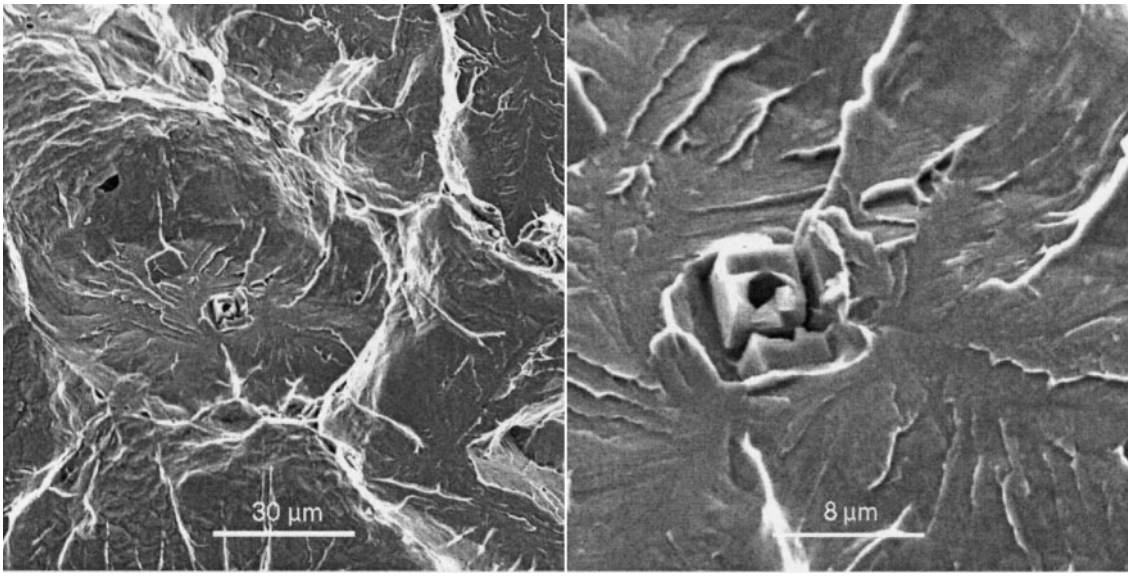

15 Fracture surfaces of fresh martensite + 14% δ-ferrite microstructure tested at −100°C showing Ti(C,N) initiated quasi-cleavage

of a weld HAZ is however far from being homogeneous and it is not known whether the presence of delta-ferrites affect the HAZ impact properties.

In supermartensitic stainless steels, five HAZ regions can be distinguished as illustrated in Fig. 19:[2]

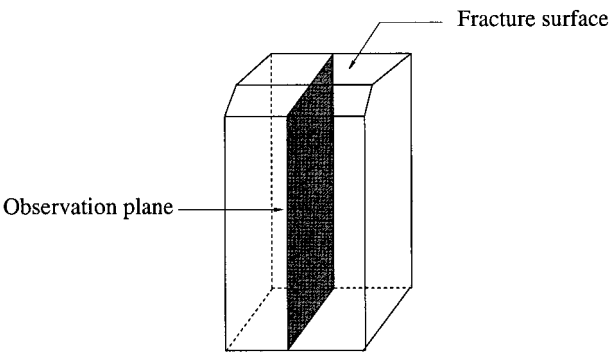

16 Location of transverse section in Charpy specimens

(i) partially melted region, located beside the fusion boundary. This is where incipient melting of the newly formed δ-ferrite occurs on heating
(ii) region which transforms completely to δ-ferrite on heating with significant grain growth, also called the coarse-grained HAZ (CG-HAZ)
(iii) high-temperature two-phase region characterised by partial transformation of austenite to δ-ferrite on heating
(iv) region which completely transforms to austenite during heating
(v) a low peak temperature two-phase region, characterised by partial transformation of the tempered martensite to austenite during heating.

The HAZ represents the area where all phase transformations occur in the solid state and therefore the partially melted region should not be regarded as belonging to the HAZ. The other regions can be artificially classified into two categories depending on the maximum temperature they experienced before cooling, the high temperature and the low temperature HAZ. The high temperature HAZ

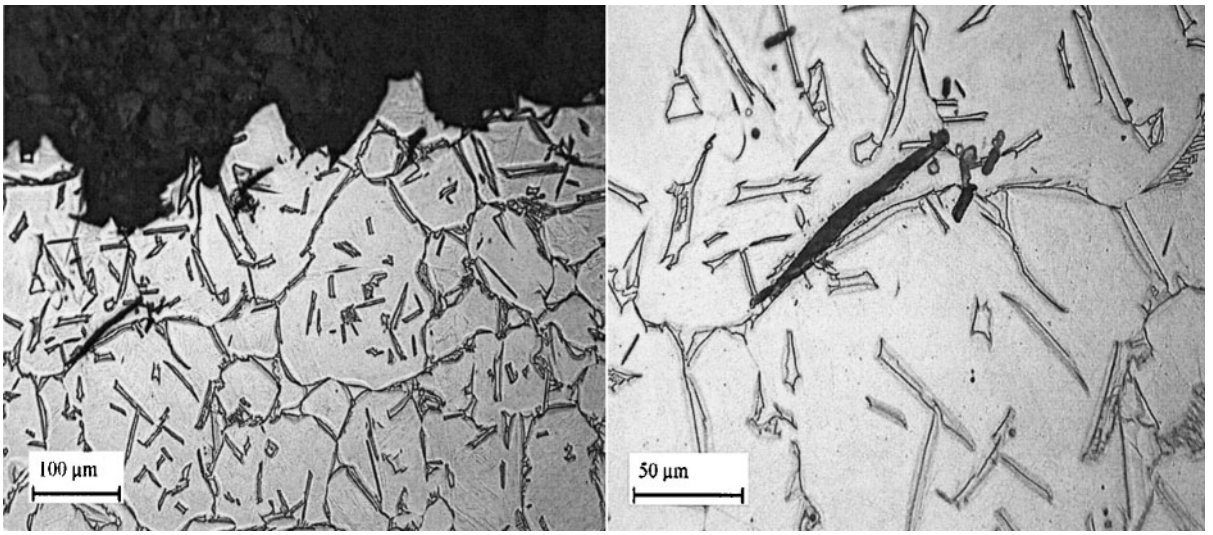

17 Cross-section of fracture surface of fresh martensite + 14% δ-ferrite microstructure tested at −100°C. Electrolytically etched to reveal δ-ferrite

(HT-HAZ) includes the prior δ-ferrite region and the high temperature two-phase region whereas the low temperature HAZ (LT-HAZ) refers to the remainder of the HAZ. An example of a typical HAZ found in a single pass weld performed on steel A is shown in Fig. 20.

As presented in another publication, the high temperature region of a supermartensitic stainless steel HAZ is likely to contain non-equilibrium δ-ferrite.[1] High heat inputs single pass bead on plates such as the one showed in Fig. 20, yield slow cooling rates in the CG-HAZ and favour the formation of Widmanstätten austenite during cooling from the fully ferritic region. It is between the Widmanstätten austenite subunits that ferrite is found in coarse-grained HAZ.[1] In dual-phase HAZ on the other hand, ferrite is usually located at grain boundaries and as thin films within the grains. The volume fraction of δ-ferrite is dependent upon the actual welding conditions but is usually smaller in coarse-grained HAZ. This is because fast cooling rates restrict Widmanstätten austenite formation in coarse-grained HAZ but prevent ferrite dissolution in the dual-phase HAZ.[9]

Gleeble weld-simulator

Being close to the weld metal, sampling of all the HAZ regions for Charpy impact testing is difficult. To avoid this problem, a Gleeble weld-simulator has been employed. The Gleeble 1500 is a thermomechanical testing device that is used in a wide range of applications including simulation and testing of weld heat affected zones. A major advantage of the Gleeble is that it generates large volumes of microstructure that simulate small, hard to study regions in actual weldments. A range of specimen geometries can be used, but by using bars, Charpy specimens can directly be machined after simulation.

The machine (Fig. 21) is interfaced to a computer that is readily programmed to provide reference signals for closed-loop control of the applied thermal cycle. Heating is accomplished by the flow of low-frequency alternating current in the specimen. The current distribution is controlled by the cross-section of the specimen and the jaws used to mount it. The feedback signal necessary for closed-loop control is obtained from a thermocouple welded to the specimen surface.[21]

Procedure

Ten specimens of dimension $11 \times 11 \times 100$ mm (taken according to Fig. 2) were machined for HAZ simulation. The operation was performed at the maximum temperature

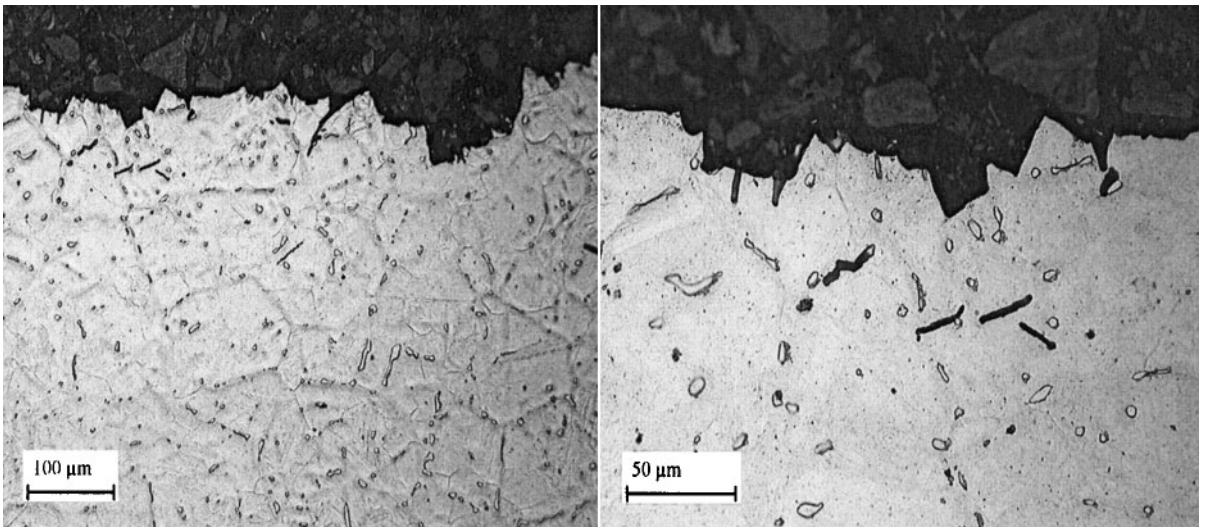

18 Cross-section of fracture surface of fresh martensite + 2% δ-ferrite microstructure tested at −150°C. Electrolytically etched to reveal δ-ferrite

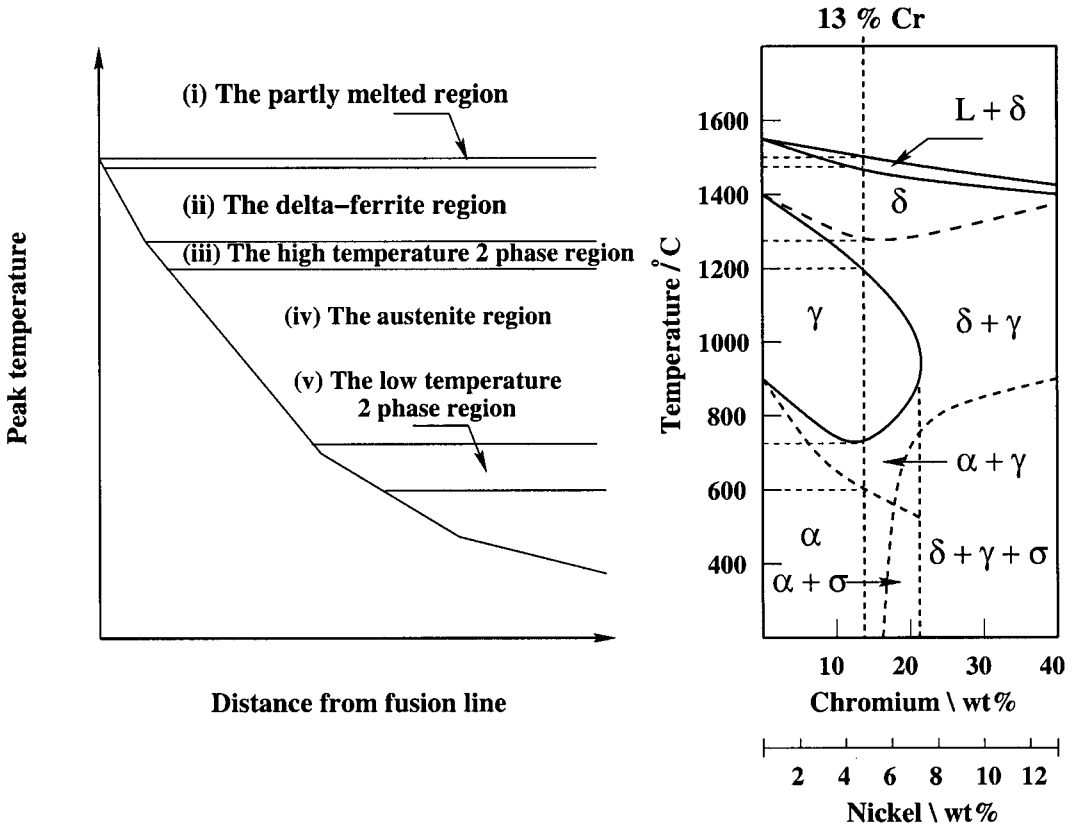

19 Schematic diagram illustrating structural changes that occur within heat affected zone of single-pass supermartensitic stainless steel weld[2]

of 1350°C using a cooling time between 800 and 500°C of 10 s. After simulation, all specimens were polished and etched to reveal the underlying microstructure. Standard size Charpy specimens were finally machined with the notch lying across the centre of the simulated specimens.

Microstructure

Figure 22 shows a representative macrograph of the simulated specimens before grinding and polishing.

After polishing and electro-etching, the central region of all simulated specimens showed a microstructural gradient. The latter indicated an inhomogeneous thermal experience across the sample sections and might have been caused by an improper contact between the samples and the grips in the Gleeble machine. As Fig. 23*a* shows, the central region of the simulated specimens consisted of three distinct areas. The upper region had semi-circular shape and depth of about 2·5 mm and was identified as the coarse-grained region (Fig. 23*b*). The latter was surrounded by

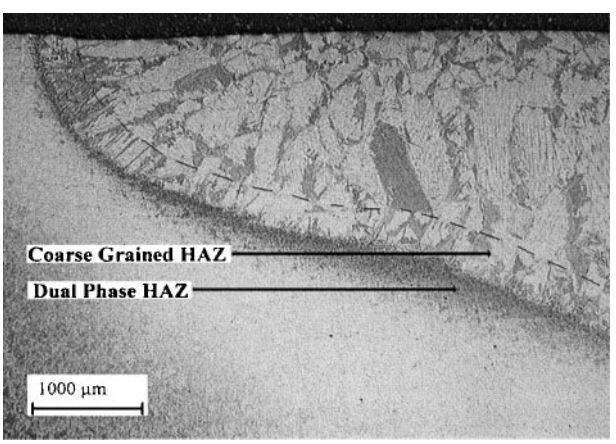

20 Optical micrograph of single-pass bead on plate performed on steel A using tungsten inert gas (TIG) process with heat input of 1 kJ mm^{-1}. Plate thickness 10 mm. Etched electrolytically to reveal δ-ferrite

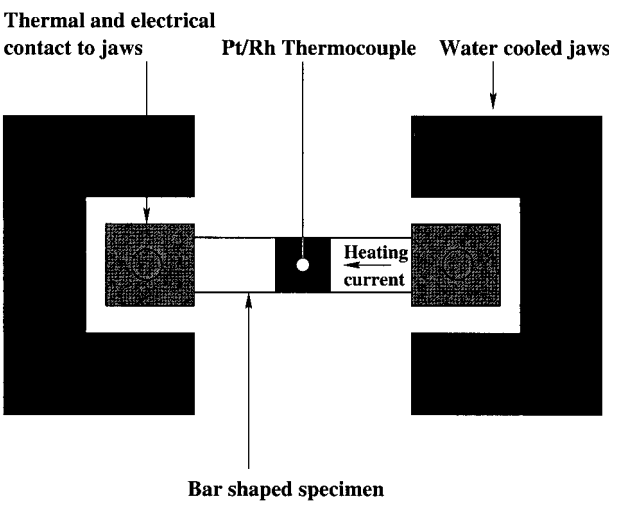

21 Arrangement of equipment within Gleeble simulator

22 Macrograph of typical specimen after HAZ simulation using Gleeble simulator. Thermocouple employed to record temperature was located at middle of centre line

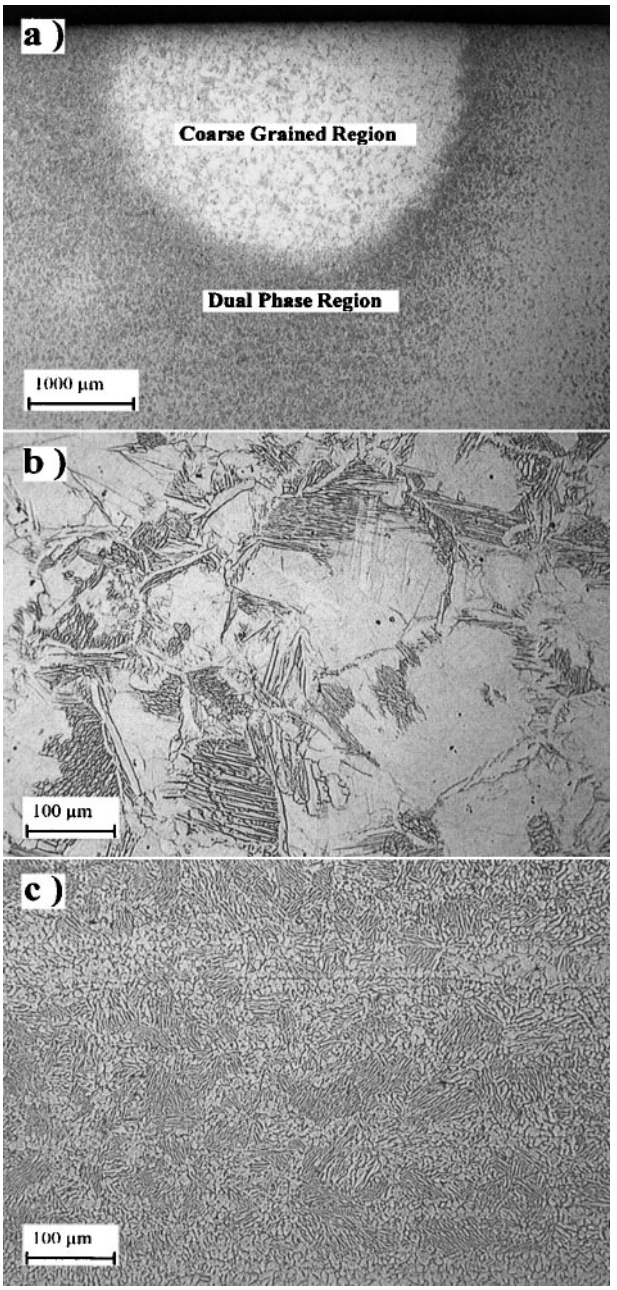

23 Microstructure of Gleeble simulated specimens; *a* low magnification of central region; *b* close-up of coarse-grained region and *c* close-up of dual-phase region. All specimens were electrolytically etched to reveal δ-ferrite

the dual-phase region (Fig. 23*c*), and in turn was surrounded by the prior fully-austenitic area. The existence of this microstructural gradient was not expected but it was decided to study its impact properties since the generated centre line microstructure was representative of that of a real weld HAZ.

The coarse-grained and dual-phase regions had grain size of about 160 µm and 30 µm, respectively. The δ-ferrite volume percentage in the dual-phase region measured by image analysis at a magnification of 200 (Fig. 23*c*) was $40 \pm 5\%$. This was larger than the volume percentage measured in heat treated specimens (Fig. 7*b* and *c*).

Results of Charpy impact test

The transition curve obtained on the Gleeble simulated specimens is presented in Fig. 24. For comparison, the

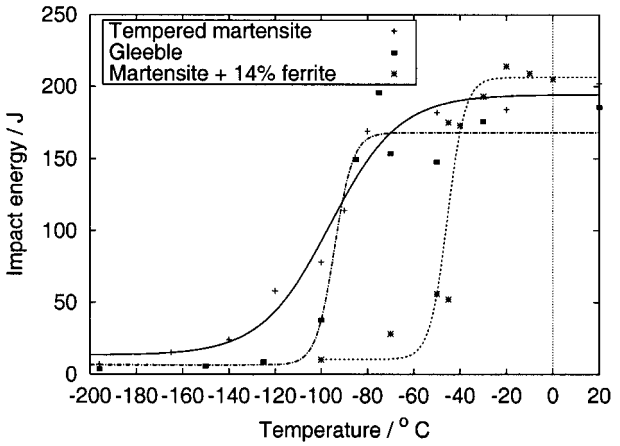

24 Charpy impact energy curve of Gleeble simulated specimens and comparison with those of as-received and fresh martensite + 14% δ-ferrite microstructures

results obtained on the as-received and martensitic/ferritic microstructures have been reported. The Gleeble specimens had the lowest upper shelf energy of the three curves. The latter was probably because of the combined action of large grain size and presence of δ-ferrite in the tested microstructure. More importantly, the simulated HAZ had a ductile to brittle transition temperature comparable to that of the as-received material (−94 and −98°C, respectively) although like the martensitic microstructure containing 14% δ-ferrite, the transition occurred over a shorter temperature range. The behaviour of the Gleeble simulated specimens at low temperatures was therefore significantly better than the ferritic/martensitic microstructure studied in the first part.

Fractography

All specimens tested at temperatures above −100°C showed ductile failure mode whereas those broken at temperatures below −100°C showed completely brittle behaviour. Interestingly, the Gleeble specimen tested at −100°C showed two fracture modes (Fig. 25). Observation of a cross-section revealed the coarse-grained region to fail by cleavage whereas the dual-phase region showed evidence of ductility below the transition temperature (Fig. 26). The ductility of the dual-phase HAZ indicates that the DBTT of this region is lower than −100°C. These results provide evidence to support the view that the presence of δ-ferrite in dual-phase HAZ up to 40% does not significantly affect the impact properties of the whole high temperature HAZ. The specimen transition temperature was more strongly influenced by the large grain size of the coarse-grained HAZ.

SUMMARY AND CONCLUSION

This work revealed that for a similar strength, particle volume-fraction and distribution, and a given prior austenite grain size, the ductile to brittle transition temperature was very sensitive to the volume fraction of δ-ferrite in homogeneous microstructures. On the other hand, tests carried out on simulated HAZ indicated that the dual-phase region did not play a major role in determining the DBTT even when δ-ferrite was present up to 40%. The small grain size of the dual-phase region offers suitable obstacles to crack propagation. Conversely, the large grain size of the coarse-grained region strongly influences the impact properties of the high temperature HAZ. However, when compared with the tempered parent material containing austenite, the transition temperature of the Gleeble simulated specimens was raised by only a few degrees. Considering that the microstructure observed in simulated

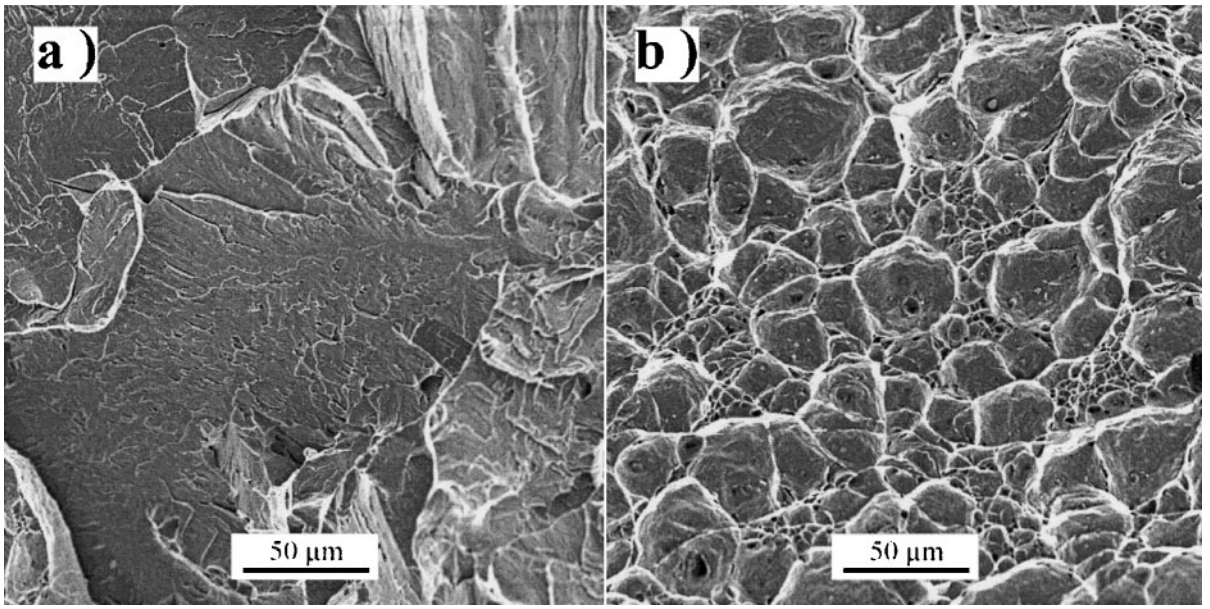

25 Fracture surfaces of *a* coarse-grained and *b* dual-phase region of Gleeble simulated specimen tested at −100°C

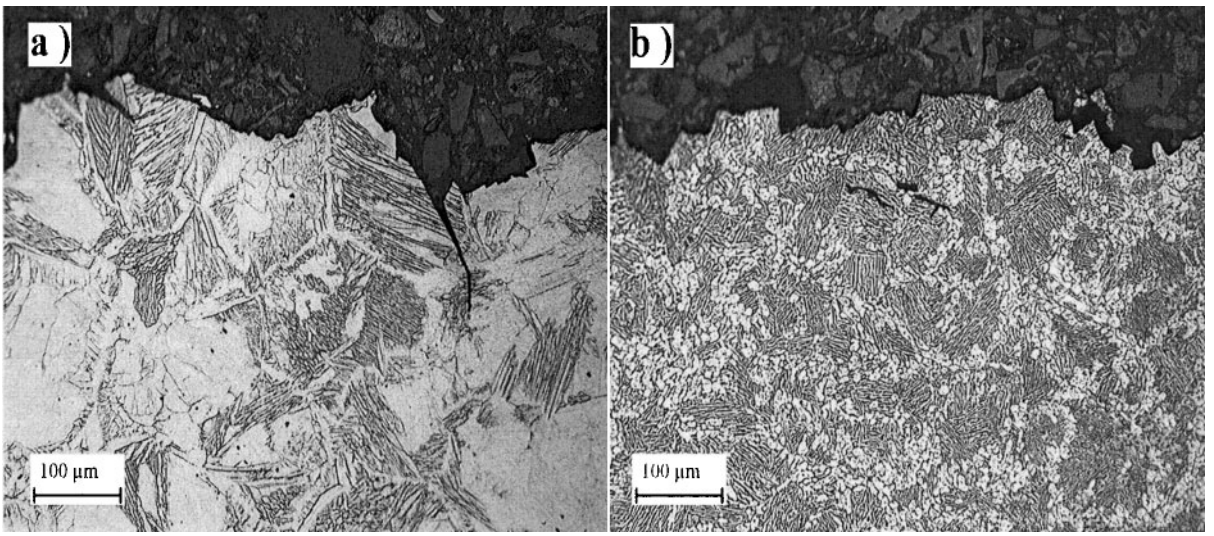

26 Cross-section of fracture surface shown in Fig. 25; *a* coarse-grained and *b* dual-phase region. This cross-section was taken perpendicular to examination plane shown in Fig. 16

HAZ is always coarser than that found in a multipass girth weld, and that the DBTT of the simulated specimens was well below room temperature, the presence of δ-ferrite in HAZ of supermartensitic stainless steels is not likely to constitute a threat to the impact properties.

ACKNOWLEDGEMENTS

The authors are grateful to TWI and the EPSRC for sponsoring this research.

REFERENCES

1. D. CARROUGE and P. WOOLLIN: in 'Stainless steel world 2002', 61–67; 2002, Houston, USA.
2. J. ENERHAUG, Ø. GRONG and U. M STEINSMO: *Sci. Technol. Weld. Joining*, 2001, **6**, 330–338.
3. T. G. GOOCH and B. J. GINN: 'Heat affected zone toughness of MMA welded 12%Cr martensitic-ferritic steel'. Technical Report 373, Welding Institute Members Report, 1988.
4. C. GROBLER: 'Weldability studies on 12% and 14% chromium steels'. PhD thesis, University of Pretoria, 1987.
5. J. J. J. ZAAYMAN and G. T. VAN ROOYEN: Proc. 1st Int. Chromium Steels and Alloys Congress, Volume 2, SAIMM, Cape Town, Johannesburg, 1992, 137–142.
6. K. KONDO, M. UEDA, K. OGAWA, H. AMAYA, H. HIRATA and H. TAKABE: in 'Supermartensitic stainless steels 99', 11–18; 1999, Belgium.
7. T. G. GOOCH, P. WOOLLIN and A. G. HAYNES: in 'Supermartensitic stainless steels 99', 188–195; 1999, Belgium.
8. P. WOOLLIN and D. CARROUGE: in 'Supermartensitic stainless steels 2002', 199–204; 2002, Paper 027.
9. D. CARROUGE: PhD thesis, Department of Materials Science and Metallurgy, University of Cambridge, 2002. Available from http://www.msm.cam.ac.uk/phasetrans/2000/phd.html#dominique.
10. P. WOOLLIN: 'Metallurgical examination of martensitic stainless steel weldments'. Technical Report 620886/1/95, Welding Institute Internal Report, 1995.
11. E. BERAHA and B. SHPIGLER: 'Color metallography'; 1977, American Society for Metals.
12. B. D. CULLITY: 'Elements of X-ray diffraction'; 1978, Addison-Wesley.
13. BS EN 10045-1. 'Charpy impact test on metallic materials. Part 1: Test method'. British Standard, 1990.
14. D. WILLIAM and J. R. CALLISTER: 'Materials science and engineering an introduction'; 1999, New York, USA, John Wiley and Sons, Inc.
15. W. OLDFIELD: CSNI Specialists Meeting on 'Instrumented precracked Charpy testing', Palo Alto, CA, 1981, 5–59.

16. P. D. BILMES, M. SOLARI and C. L. LLORENTE: *Mater. Characterisation*, 2001, **46**, 285–296.
17. R. D. KNUTSEN and R. HUTCHINGS: *Mater. Sci. Technol.*, 1988, **4**, 127–135.
18. M. M. MCDONALD and D. C. LUDWIGSON: *J. Test. Eval.*, 1983, **11**, 165–173.
19. D. P. FAIRCHILD, D. G. HOWDEN and W. A. T. CLARK: *Metall. Mater. Trans. A*, 2000, **31A**, 641–652.
20. D. P. FAIRCHILD, D. G. HOWDEN and W. A. T. CLARK: *Metall. Mater. Trans. A*, 2000, **31A**, 653–667.
21. R. D. CAMPBELL and D. W. WALSH: *ASM Metals Handbook*, 1971, **6**, 603–613.